actuators

MDPI

Article

Analysis of Current Ripples in Electromagnetic Actuators with Application to Inductance Estimation Techniques for Sensorless Monitoring

Niklas König *, Matthias Nienhaus and Emanuele Grasso

Laboratory of Actuation Technology, Saarland University, 66123 Saarbrücken, Germany; nienhaus@lat.uni-saarland.de (M.N.); grasso@lat.uni-saarland.de (E.G.)

* Correspondence: koenig@lat.uni-saarland.de

Received: 13 January 2020; Accepted: 4 March 2020; Published: 6 March 2020

Abstract: Techniques for estimating the plunger position have successfully proven to support operation and monitoring of electromagnetic actuators without the necessity of additional sensors. Sophisticated techniques in this field make use of an oversampled measurement of the rippled driving current in order to reconstruct the position. However, oversampling algorithms place high demands on AD converters and require significant computational effort which are not desirable in low-cost actuation systems. Moreover, such low-cost actuators are affected by eddy currents and parasitic capacitances, which influence the current ripple significantly. Therefore, in this work, those current ripples are modeled and analyzed extensively taking into account those effects. The Integrator-Based Direct Inductance Measurement (IDIM) technique, used for processing the current ripples, is presented and compared experimentally to an oversampling technique in terms of noise robustness and implementation effort. A practical use case scenario in terms of a sensorless end-position detection for a switching solenoid is discussed and evaluated. The obtained results prove that the IDIM technique outperforms oversampling algorithms under certain conditions in terms of noise robustness, thereby requiring less sampling and calculation effort. The IDIM technique is shown to provide a robust position estimation in low-cost applications as in the presented example involving a end-position detection.

Keywords: electromagnetic actuators; position estimation; self-sensing; sensorless; solenoid

1. Introduction

Electromagnetic actuators are nowadays widely applied in industrial, automotive, and consumer applications. In particular, single-phase reluctance actuators with proportional or switching positioning characteristic, such as valves, relays, and solenoids, are used in high quantities due to their low price. Such kinds of actuators are based on a simple and robust construction while high strokes and high forces are obtained. In the last few years, there is an increasing interest in condition monitoring and predictive maintenance mainly under the term of Industry 4.0. Such trends also involve the reluctance actuators mentioned above with the aim of obtaining reliable position information for various control and monitoring applications [1–3]. Most of the above-mentioned actuators do not include a position sensor since sensors increase significantly the system cost, size, and complexity. Only high-quality products include sensors such as encoders, linear variable differential transformers (LVDTs) or mechanical switches used for end-position detection. Nevertheless, such solutions seem inadequate in the field of low-cost actuators. Moreover, even high-quality applications with sensors require redundant position information in case high functional safety is desired [4].

The problem of an inherent position sensing is addressed by the so-called sensorless techniques, a field that is widely known for decades in the case of electrical machines [5–9]. Common approaches

for machines make use of two physical effects: the evaluation of the back-induced electromotive force (back-EMF) [5] and the exploitation of the position-dependent inductance [6–9]. Techniques using back-EMF information mainly make use of observers and are applicable only for middle and high-speed applications, thus making this approach unsuitable for solenoids used in positioning applications. On the other hand, techniques using the inductance information allow position estimation even in standstill conditions, making such kinds of techniques appropriate for solenoids. Remarkable works in this field are based on the injection of voltage test signals in order to estimate the inductance and then, in a further step, the position. In the field of rotating machines, a renowned work was made by Schroedl on the so-called INdirect Flux detection by On-line Reactance Measurement (INFORM) approach [6]. In this work, voltage test pulses are applied and the resulting current rise is measured. From the evaluation of the current rise, a precise inductance and position estimation is possible. Other techniques [7–9] go under the term of high frequency current injection (HFCI), since they are injecting a high-frequency voltage carrier into the actuator. By measuring and demodulating the resulting current, an inductance and, therefore, position estimation is possible.

Inspired by the success of sensorless control for rotating machines, similar approaches arose also for solenoid actuators. In particular, the works [10,11] show the observer approach applied to solenoids while the works [3,12] show the successful application of the injection-based approach. Nevertheless, the injection-based techniques suffer from several disadvantages: due to the injection of an harmonic signal into the actuator, a considerable acoustic noise as well as a force ripple is generated while power losses inside the system are increased. Furthermore, the applicable driving voltage is reduced by the superposition of an injection signal and the dynamic working range is reduced, since the mechanical movement must be considerably slower than the frequency of the injection signal. Hence, more sophisticated works exploit the current variation caused by the use of a switching power electronics operated under Pulse Width Modulation (PWM). Such ripple is inherently present inside the actuator, and no further signal injection is required.

Works exploiting and analyzing the current ripple in reluctance actuators are mainly divided into three categories: derivative-based methods, oversampling methods, and analog signal processing methods. Derivative-based works such as [13–17] measure the current ripple in order to calculate numerically the current derivative, which is strictly linked to the inductance. By considering a 2nd order derivative, a compensation of the resistive effect and the back-EMF is possible. Nevertheless, a significant demerit of those techniques is the robustness and the signal-to-noise ratio (SNR) of the obtained estimate, since the derivative of a current measurement, usually affected by noise, is calculated. This becomes more significant in applications exhibiting small currents and small inductance variations. Moreover, those techniques calculate the derivative by assuming a linear slope of the current ripple, which is usually exponentially shaped. Due to its demerits, these kinds of techniques are not considered here. In order to increase the SNR significantly, other works [18–22] make use of an oversampled current measurement with a sampling rate significantly higher than the PWM frequency. Based on the obtained data set, a regression or a curve fitting of the current ripple allows the identification of the inductance. This leads to a precise and robust measurement of the inductance with high SNR. Nevertheless, the oversampled measurement and the required data processing, usually based on least-mean squares methods, require high computational and sampling effort. For instance, the work [21] requires 10 k Samples per each PWM period. This makes the implementation of such techniques expensive and, therefore, unacceptable in low-cost applications like solenoids. The last category based on hardware signal processing tries to decrease computational effort by pre-processing the signals through an analog electronics: the hysteresis amplifier in [23] offers a simple method for estimating the inductance. Nevertheless, it requires a linear power electronics instead of a switching power electronics, making this solution unsuitable in terms of energy efficiency. The work [24] makes use of an analog demodulation unit consisting of a high-pass filter, a rectifier, and a low-pass filter. This allows an estimate of inductance within analog electronics, with the demerit of a limitation in dynamics.

The above-mentioned techniques show that the use of a pre-processing hardware increases the SNR while minimizing the computational effort. This inspired the works [25–27] introducing the so-called Integrator-Based Direct Inductance Measurement (IDIM) technique, which makes use of an analog integrator for inductance estimation: due to the concept of analog integration, the current ripple can be amplified while the noise is rejected during integration. While [25,26] presented the basic concept of the IDIM approach with several restrictions on the current dynamics, Ref. [27] proposed an approach without any restriction on the dynamics. The IDIM technique is successfully applied to electromagnetic reluctance actuators and its accuracy and applicability is successfully shown in the above-mentioned works. In particular, the improved approach is verified on an electromagnetic levitation system with closed-loop position control.

Nevertheless, solenoid actuators usually exhibit significant parasitic effects such as eddy currents, especially due to non-laminated ferromagnetic materials, and parasitic capacitances due to a high number of windings. Such effects represent a major limitation in actuators since they significantly influence the induced current ripple. Therefore, the following work offers a thorough analysis of the current ripple inside an electromagnetic reluctance actuator including parasitic effects such as iron losses, eddy currents, and capacitances as well as back-EMF voltages and improves the mathematical description of the IDIM technique taking into account the presence of those effects. Another important research aspect concerns noise rejection and computational effort of the discussed techniques. In general, oversampling approaches guarantee a robust identification with high SNR as long as a sufficiently large numbers of samples is given, thus leading to a significant increase in measurement and computational effort. It is of interest to compare these kinds of techniques to the IDIM technique in terms of noise robustness and needed measurement effort in order to find the trade-off-point between oversampling approaches with different numbers of samples and the IDIM technique. Therefore, an experimental set-up with an industrial solenoid actuator is used to identify and compare the noise power of the estimated inductance in case the IDIM technique or an oversampling algorithm is used. Finally, in order to prove the performance of the IDIM technique in the case of a low-cost actuation system, the technique is applied to a practical use case scenario: the position estimated by the sensorless technique is used for end-position detection in a solenoid actuator with switching behavior in order to detect whether the actuator has opened or closed successfully. The obtained sensorless position estimator is compared to the position measured by an high-precision positioning table and conclusions concerning precision, noise robustness, and implementation effort are drawn.

2. Mathematical Analysis of the Current Ripples inside Electromagnetic Actuators

A generic electromagnetic actuator and its parasitic effects can be modeled by the electrical equivalent circuit shown in Figure 1, as proposed in the work [23]. In particular, the model contains a series resistance R_s, due to the copper wire and connectors, as well as an inductance L. The parallel resistance R_p represents dissipative elements in the actuator such as iron losses like eddy currents. Additionally, a capacitive coupling between the actuator windings, housing, and plunger are modeled by the parallel capacitance C_p. The voltage source u_{BEMF} denotes the back-EMF induced inside the actuator during motion. The voltage u is the driving voltage present at the actuator terminals while the current i_s stands for the total current flowing through the actuator.

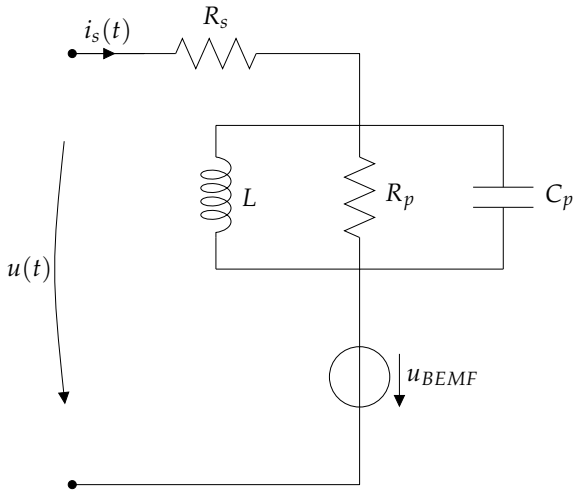

Figure 1. Electrical equivalent circuit of a generic electromagnetic actuator.

In the particular case of reluctance-based electromagnetic actuators such as solenoids, where no permanent magnets are present, the discussed electrical equivalent circuitry can be simplified by making a consideration on the back-EMF voltage u_{BEMF}. Thus, by considering the flux Ψ inside the actuator:

$$u(t) = \frac{d\Psi(t)}{dt} = u_L(t) + u_{BEMF}(t) = L \cdot \frac{di_s(t)}{dt} + \frac{dL}{dt} \cdot i_s(t) = L \cdot \frac{di_s(t)}{dt} + \frac{dL}{dx} \cdot \frac{dx}{dt} \cdot i_s(t), \quad (1)$$

it can be seen that the back-EMF inside the actuator has a linear dependency on the current. Therefore, the back-EMF can be represented as a resistive component, depending on the position x and the speed v of the actuator. Therefore, the total resistance R_Σ of the actuator can be defined as:

$$R_\Sigma = R_s + \frac{dL}{dx} \cdot v \cdot i_s(t). \quad (2)$$

Electromagnetic actuators are usually driven by switching power electronics such as H-bridges and, therefore, are driven with a bipolar PWM voltage, which can be described mathematically as:

$$u_{pwm}(t) = \begin{cases} +U_{DC} & \text{for} \quad 0 \leq t \leq \alpha \cdot t_{pwm} \\ -U_{DC} & \text{for} \quad \alpha \cdot t_{pwm} \leq t \leq t_{pwm} \end{cases}, \quad (3)$$

where U_{DC} is the DC-link voltage of the used power electronics, t_{pwm} is the PWM time period and α denotes the applied duty cycle, which is limited to a value between 0% and 100%: $\alpha \in [0, 1]$. The driving of the actuator with such a bipolar PWM voltage inherently introduces a current ripple, which overlaps the fundamental current of the actuator. This ripple can be seen as the periodic partial charging and discharging of the inductor. Therefore, the current ripple excites the inductance in the small signal range around its actual working point, leading to the presence of the so called differential inductance L_d. Thus, together with the consideration on the back-EMF, the electrical equivalent circuit of a reluctance-based actuator can be simplified, as shown in Figure 2.

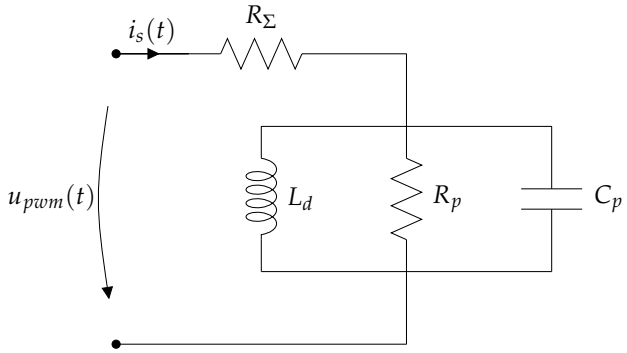

Figure 2. Reduced electrical equivalent circuit in case of a reluctance-based actuator which is driven by a PWM voltage.

By applying Kirchhoff's rules, the differential equation of the circuitry can be obtained:

$$u(t) + \frac{L_d}{R_p} \cdot \frac{du(t)}{dt} + L_d \cdot C_p \cdot \frac{d^2u(t)}{dt} = R_\Sigma \cdot i_s(t) + L_d \cdot \left(1 + \frac{R_\Sigma}{R_p}\right) \cdot \frac{di_s(t)}{dt} + C_p \cdot R_\Sigma \cdot L_d \cdot \frac{d^2i_s(t)}{dt}. \quad (4)$$

In particular, the differential equation contains the parameters $R_\Sigma(T, v)$, $L_d(x)$, $R_p(x)$ and $C_p(x)$, which usually vary over time due to mechanical movement or temperature change. Indeed, this work exploits the position dependence of the differential inductance L_d. Nevertheless, those parameters can be assumed constant over one PWM period t_{pwm} in order to simplify the analytical solution of that differential equation. This assumption holds for most actuators due to the fact that the mechanical time constant and the thermal time constant are several orders of magnitude higher than the electrical time constant and the applied PWM period.

2.1. Analysis of the Response of a RL Circuit Driven with a PWM Voltage

In the first step, only the resistive part R_Σ as well as the inductance L_d will be considered in the analysis of the ideal current response of an electromagnetic actuator under PWM operation. The parasitics are neglected by setting $C_p = 0$ and $R_p \to \infty$, thereby leading to the differential equation:

$$u(t) = R_\Sigma \cdot i_s(t) + L_d \cdot \frac{di_s(t)}{dt}. \quad (5)$$

The solution of the differential equation given an input $u(t)$ equal to zero is:

$$i_s(t) = i_s(0) \cdot e^{-\frac{R_\Sigma}{L_d} \cdot t}, \quad (6)$$

where the initial current in the coil is denoted as $i_s(0)$. Solving the differential Equation (5) for the piecewise-defined PWM input shown in Equation (3), in particular where $u(t) = u_{pwm}(t)$ and therefore $u(t) = U_{DC}$ for $0 \leq t \leq \alpha \cdot t_{pwm}$ and $u(t) = -U_{DC}$ for $\alpha \cdot t_{pwm} \leq t \leq t_{pwm}$, yields to:

$$i_s(t) = \begin{cases} \frac{1}{R_\Sigma}\left(U_{DC} + (R_\Sigma \cdot i_s(0) - U_{DC}) \cdot e^{-\frac{R_\Sigma}{L_d} t}\right) & \text{for} \quad 0 \leq t \leq \alpha \cdot t_{pwm} \\ \frac{1}{R_\Sigma}\left(-U_{DC} + (R_\Sigma \cdot i_s(\alpha \cdot t_{pwm}) + U_{DC}) \cdot e^{-\frac{R_\Sigma}{L_d}(t - \alpha \cdot t_{pwm})}\right) & \text{for} \quad \alpha \cdot t_{pwm} \leq t \leq t_{pwm} \end{cases}, \quad (7)$$

where

$$i_s(\alpha \cdot t_{pwm}) = \frac{1}{R_\Sigma}\left(U_{DC} + (R_\Sigma \cdot i_s(0) - U_{DC}) \cdot e^{-\frac{R_\Sigma}{L_d} \cdot \alpha \cdot t_{pwm}}\right). \quad (8)$$

For better understanding, this equation can be transformed into:

$$i_s(t) = \begin{cases} i_s(0) + \left(\frac{U_{DC}}{R_\Sigma} - i_s(0)\right)\left(1 - e^{\frac{-R_\Sigma \cdot t}{L_d}}\right) & \text{for} \quad 0 \le t \le \alpha \cdot t_{pwm} \\ i_s(\alpha \cdot t_{pwm}) + \left(\frac{-U_{DC}}{R_\Sigma} - i_s(\alpha \cdot t_{pwm})\right)\left(1 - e^{\frac{-R_\Sigma \cdot (t - \alpha \cdot t_{pwm})}{L_d}}\right) & \text{for} \quad \alpha \cdot t_{pwm} \le t \le t_{pwm} \end{cases}, \tag{9}$$

where the fundamental current $i_s(0)$ as well as $i_s(\alpha \cdot t_{pwm})$ can be clearly separated from the current ripple.

2.2. Analysis of the Response of the Complete Circuit Driven with a PWM Voltage

In order to analyze the behavior of an electromagnetic actuator together with its parasitics, the full differential Equation (4) including the parallel resistance R_p as well as the parasitic capacitance C_p will be considered. For sake of brevity, we skip the analytical expression and show directly the numerical solution of the differential equation. Because the numerical solver does not converge at the PWM switching points due to the lack of differentiability, a PWM switching voltage with a ramp instead of sharp edges is used for numerical simulation. The slope of this ramp is considered with a rise time of 100 ns, allowing convergence of the solver and representing typical switching times in power electronics made of field-effect transistors.

Equation (4) represents a second order system, which can be critically damped, underdamped, or overdamped based on the conditions:

$$L_d = 4R_\Sigma^2 C_p \qquad \text{critically damped} \tag{10}$$

$$L_d < 4R_\Sigma^2 C_p \qquad \text{underdamped} \tag{11}$$

$$L_d > 4R_\Sigma^2 C_p \qquad \text{overdamped} \tag{12}$$

The simulated current $i_s(t)$ inside the actuator is shown in Figure 3 for a parameter set representing the overdamped case. Figure 4 illustrates $i_s(t)$ for the case of a parameter set of an underdamped circuit. In order to highlight the influence of the parasitics, the current response without each of the parasitics is added in the figures. It must be denoted that the presented example exaggerates the parasitic capacitance for better visibility. In common electromagnetic actuators, the parasitic capacitance is usually so small [28] that, according to condition (12), the circuit can be considered as overdamped. In the over- and underdamped case, it is clearly visible that the charging current of the capacitor superimposes the classical response of the current ripple in a RL-circuit, especially at the switching instants, where overshoots occur. This effect becomes more significant in case C_p is increased. Additionally, the parallel resistance leads to a slight change in the slope of the current ripple and to a voltage jump happening at the switching instant. The height of that jump strictly depends on the value of R_p. This is due to the reason that the resistor bypasses the inductance at the switching instant, allowing eddy currents to flow directly. In reality, currents cannot rise with such an infinite slew rate due to the presence of inductances delaying those currents. Nevertheless, those inductances are usually so small that this model still provides a sufficient approximation.

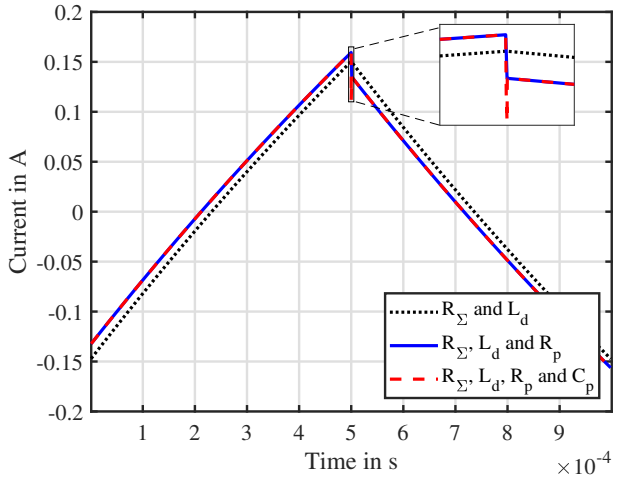

Figure 3. Simulated current inside the actuator in case of an overdamped system: $R_\Sigma = 10\ \Omega$, $L = 20$ mH, $C_p = 100$ pF, $R_p = 1000\ \Omega$, $f_{pwm} = 1$ kHz, $\alpha = 0.5$.

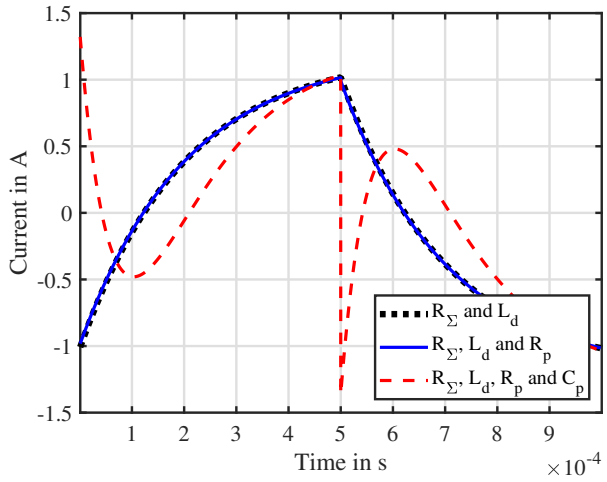

Figure 4. Simulated current inside the actuator in case of an underdamped system: $R_\Sigma = 10\ \Omega$, $L = 2$ mH, $C_p = 5.01$ µF, $R_p = 1000\ \Omega$, $f_{pwm} = 1$ kHz, $\alpha = 0.5$.

2.3. Approximation of the Model for Common Electromagnetic Reluctance Actuators

As seen above, parasitic components such as eddy currents and parasitic capacitances can play a significant role in the obtained current ripple, especially at the switching instants of the PWM voltage. Nevertheless, assumptions can be considered, which simplify the mathematical treatment significantly and which still hold on most of the common electromagnetic reluctance actuators. In the first step, the series resistance R_Σ is considered being much smaller than the parallel resistance R_p: $R_\Sigma \ll R_p$. This is due to the reason that, in the particular case of reluctance actuators, the series resistance consists of one side on the copper resistance and on the other side on the part $\frac{dL}{dx} \cdot v \cdot i_s(t)$ representing the back-EMF induced during movement. The first one is normally designed to be small in order to decrease power dissipation. The latter one, indeed, does not predominate since such actuators are made for positioning applications and not for high speed operation. In the next step, considerations are made on the parasitic capacitance C_p. In particular, the capacitive coupling between the windings as well as the housing and the plunger is so small that the system is overdamped and so small that the eigenfrequency $\frac{1}{2\pi\sqrt{L_d \cdot C_p}}$ is much higher than the PWM frequency. Therefore, the following assumption can be made: $L_d \cdot C_p \to 0$. Indeed, many works such as [23,28] neglect the

parasitic capacitances in solenoids completely. Nevertheless, the overshoot at the switching instant still occurs in the overdamped case.

3. Inductance Estimation Approaches

In the following, inductance estimation techniques will be shown, which exploit the current ripple that is derived mathematically in the previous section. Firstly, the IDIM technique is recalled and adapted in such a way that it is not influenced by the presence of parasitics. Then, a simplified IDIM technique is derived for applications that do not require high dynamics. Finally, a classical oversampling approach discussed in the state-of-the-art is briefly shown for comparison.

3.1. Integrator-Based Direct Inductance Measurement (IDIM) Approach

Figure 5 shows the analog measurement circuitry that is necessary for the implementation of the IDIM technique. The circuitry removes the fundamental current component from the sensed current signal by means of a sample and hold (S/H) stage and integrates the offset-elimated current $\bar{i}_s(t)$ over defined integration windows. By removing the offset, the current ripple containing the inductance information can be separated from the fundamental current, and, therefore, can be strongly amplified while noise is rejected.

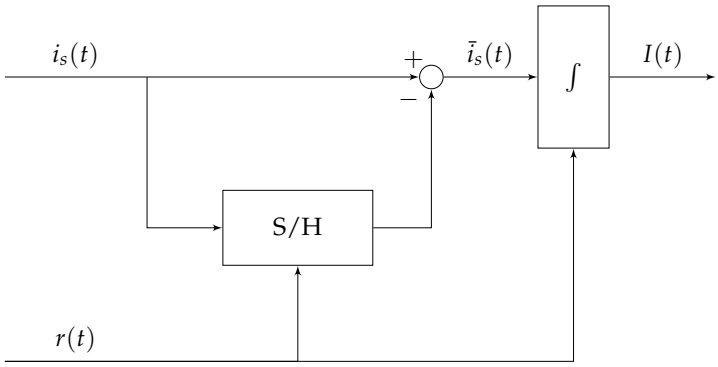

Figure 5. Circuitry used for the implementation of the IDIM technique, including an offset-eliminating stage and an analog integrator with reset capability.

The integration windows and their corresponding trigger signal $r(t)$ can be chosen in such a way that the switching instants of the PWM voltage can be avoided during integration. At these time instants, not only the direct feed-through of the first and second voltage derivative caused by R_p and C_p occur, but also nonlinear effects caused by the switching electronics such as dead-time insertion and ringing as well as glitches occur. Moreover, most current sensors suffer from limited bandwidth and slew rate in these time instants. Resetting the integrator in those time periods ensures that these effects do not influence the inductance measurement with IDIM. The avoidance of acquiring measurements in these areas is also considered in the oversampling approaches such as [21].

In order to avoid the switching instants, the trigger signal $r(t)$ can be defined as:

$$r(t) = \begin{cases} 0 & \text{for} \quad t_s^+ \leq t \leq \cdot t_e^+ \\ 0 & \text{for} \quad t_s^- \leq t \leq \cdot t_e^- \\ 1 & \text{else} \end{cases}, \tag{13}$$

with

$$t_s^+ = t_r, \qquad t_e^+ = \alpha \cdot t_{pwm}, \qquad t_s^- = \alpha \cdot t_{pwm} + t_r, \qquad t_e^- = t_{pwm} - t_r. \tag{14}$$

When $r(t)$ is equal to 0, the S/H stage holds its actual value and the integration starts and when $r(t)$ is equal to 1, the integrator is reset and the S/H stage is sampling the input. The times t_s^+ and

t_e^+ are the times of the start and the end of the integration window when the positive voltage pulse is applied, hence the times t_s^- and t_e^- refer to the ones when a negative pulse is applied. The design parameter t_r should be chosen sufficiently long to ensure that the disturbances caused by the voltage switching are decayed and the integrator is fully reset. The integrator stage with embedded reset capability can be realized by a fully differential operational amplifier with electronic switches parallel to the integrator capacitor C_{int}, as shown in Figure 6.

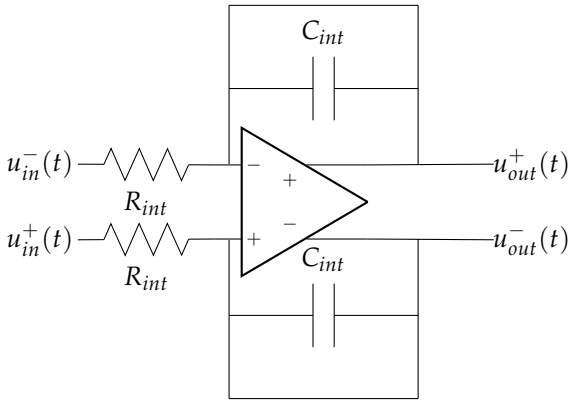

Figure 6. Fully differential analog integrator with reset capability.

Its transfer characteristics can be described analytically as follows:

$$u_{out}(t) = -\frac{1}{R_{int}C_{int}} \int_{r(t)\neq 1} u_{in}(t)dt, \tag{15}$$

where $u_{in}(t)$ is the output voltage of a current sensor. For better comprehension, the current sensor and its transfer function will be not considered here and the mathematical description will directly focus on the sensed current. The term $\frac{1}{R_{int}C_{int}}$ represents the integration gain, which has to be chosen carefully by the user in order to avoid saturation of this stage. For sake of brevity, this gain is set to 1 in the following derivations. Due to the periodic reset, the integrator does not suffer from offsets or drifts. The output of the integrator stage with respect to the given trigger signal $r(t)$ is shown exemplarily in Figure 7 for a current ripple caused by a PWM voltage with a duty cycle α of 0.5.

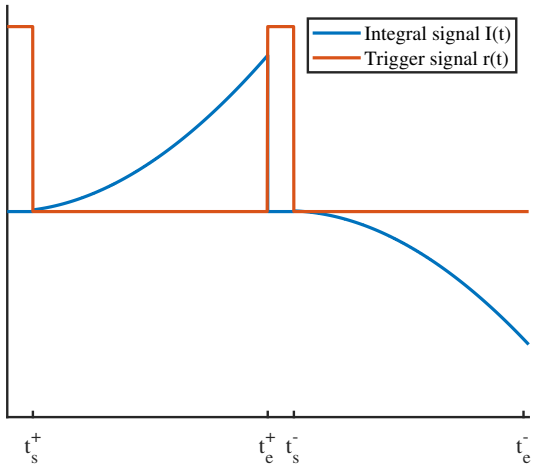

Figure 7. Integral obtained by the IDIM circuit (blue), trigger signal $r(t)$ (red) as well as time instants, exemplary shown for $\alpha = 0.5$.

Based on the illustrated integrator circuitry, the integral of the current ripple can be defined as:

$$I(t) = \int_{r(t)\neq 1} \bar{i}_s(t)dt = \int_{r(t)\neq 1} (i_s(t) - i_s(t_x))dt, \tag{16}$$

which can be rewritten by considering Equation (4) as

$$\begin{aligned} I(t) = \int_{r(t)\neq 1} (\frac{1}{R_\Sigma}(u(t) + \frac{L_d}{R_p}\cdot\frac{du(t)}{dt} + L_d\cdot C_p\cdot\frac{d^2u(t)}{dt} - L_d\cdot\left(1+\frac{R_\Sigma}{R_p}\right)\cdot\frac{di_s(t)}{dt} \\ -C_p\cdot R_\Sigma\cdot L_d\cdot\frac{d^2i_s(t)}{dt}) - i_s(t_x))dt, \end{aligned} \tag{17}$$

where t_x represents the time where the S/H stage holds, in particular t_s^+ for the positive voltage pulse and t_s^- for the negative voltage pulse. This expression can be evaluated for the given voltage shown in Equation (3), exemplary shown for the positive voltage pulse:

$$\begin{aligned} I(t_e^+) - I(t_s^+) = \frac{U_{DC}}{R_\Sigma}\left(t_e^+ - t_s^+\right) + \frac{L_d}{R_\Sigma R_p}\left(u(t_e^+) - u(t_s^+)\right) + \frac{L_d C_p}{R_\Sigma}\left(\frac{du(t_e^+)}{dt} - \frac{du(t_s^+)}{dt}\right) \\ -\frac{L_d}{R_\Sigma}\left(1+\frac{R_\Sigma}{R_p}\right)(i_s(t_e^+) - i_s(t_s^+)) - C_p L_d\left(\frac{di_s(t_e^+)}{dt} - \frac{di_s(t_s^+)}{dt}\right) - i_s(t_s^+)(t_e^+ - t_s^+). \end{aligned} \tag{18}$$

This expression allows for calculating the output of the IDIM circuitry shown in Figure 5 taking into account the presence of the parasitics. Since the integrator is reset at the start of the integration, the initial value of the integral can be set to zero : $I(t_s^+) = 0$. By using the approximations $R_\Sigma \ll R_p$ and $L_d \cdot C_p \to 0$ mentioned in Section 2.3 and by evaluating the function values of the given input voltage $u(t_e^+) = u(t_s^+) = U_{DC}$ and $\frac{du(t_e^+)}{dt} = \frac{du(t_s^+)}{dt} = 0$, the equations can be simplified to:

$$I(t_e^+) \approx \frac{U_{DC}}{R_\Sigma}(t_e^+ - t_s^+) - \frac{L_d}{R_\Sigma}(i_s(t_e^+) - i_s(t_s^+)) - i_s(t_s^+)(t_e^+ - t_s^+). \tag{19}$$

Analogically, the expression for the negative pulse can be obtained:

$$I(t_e^-) \approx -\frac{U_{DC}}{R_\Sigma}(t_e^- - t_s^-) - \frac{L_d}{R_\Sigma}(i_s(t_e^-) - i_s(t_s^-)) - i_s(t_s^-)(t_e^- - t_s^-). \tag{20}$$

Equations (19) and (20) can be merged into a matrix form:

$$\begin{bmatrix} U_{DC}(t_e^+ - t_s^+) \\ -U_{DC}(t_e^- - t_s^-) \end{bmatrix} \approx \begin{bmatrix} I(t_e^+) + i_s(t_s^+)(t_e^+ - t_s^+) & i_s(t_e^+) - i_s(t_s^+) \\ I(t_e^-) + i_s(t_s^-)(t_e^- - t_s^-) & i_s(t_e^-) - i_s(t_s^-) \end{bmatrix} \begin{bmatrix} R_\Sigma \\ L_d \end{bmatrix}, \tag{21}$$

$$\begin{bmatrix} U_{DC}(t_e^+ - t_s^+) \\ -U_{DC}(t_e^- - t_s^-) \end{bmatrix} \approx \mathbf{A}\begin{bmatrix} R_\Sigma \\ L_d \end{bmatrix}, \tag{22}$$

allowing the calculation and analysis of the determinant of matrix **A**:

$$|\mathbf{A}| = (I(t_e^+) + i_s(t_s^+)(t_e^+ - t_s^+))(i_s(t_e^-) - i_s(t_s^-)) - (I(t_e^-) + i_s(t_s^-)(t_e^- - t_s^-))(i_s(t_e^+) - i_s(t_s^+)). \tag{23}$$

The determinant must be always unequal to zero for determining the parameters of R_Σ and L_d. It can be shown that the determinant is equal to zero, e.g., when there is zero mean current. Without a current in the coil, an identification of the resistance R_Σ becomes impossible, thus L_d cannot be identified correctly. In such cases, a pre-identified value of R_Σ has to be used for the estimation of L_d. In that situation, the mean current equals zero; therefore, according to Equation (2), no back-EMF is present and R_Σ equals the series resistance R_s, which can be pre-identified using standard resistance measurement techniques, such as a recursive least squares (RLS) based identifier [29].

In case the matrix **A** is invertible, the parameters R_Σ and L_d can be estimated by the expressions:

$$R_\Sigma \approx \frac{U_{DC}}{|A|}((i_s(t_e^-) - i_s(t_s^-))(t_e^+ - t_s^+) + (i_s(t_e^+) - i_s(t_s^+))(t_e^- - t_s^-)), \tag{24}$$

$$L_d \approx -\frac{U_{DC}}{|A|}((I(t_e^-) + i_s(t_s^-)(t_e^- - t_s^-))(t_e^+ - t_s^+) + (I(t_e^+) + i_s(t_s^+)(t_e^+ - t_s^+))(t_e^- - t_s^-)). \tag{25}$$

Since the resistance R_Σ is actively identified and compensated in the estimation of the differential inductance, a back-EMF or a change of the resistance due to heating can be compensated. Additionally, it can be seen that this technique requires in total seven measurements per PWM period: one DC link voltage measurement, measurements of the integrator at two time instants per each PWM period, and current measurements at four time instants per each PWM period. The estimate of inductance and resistance can be obtained by solving two closed equations. Nevertheless, those equations contain current differences, whose calculation might increase the noise power of the estimate.

3.2. Simplified IDIM Approach

The simplified IDIM technique neglects the effect of the parallel resistance R_p as well as the parallel capacitance C_p and assumes that the actuator is driven with a low current dynamic. This is especially suitable for end-position detection for switching actuators, where the position is determined after the switching in a quasi-static manner. The following derivation resembles the work [25].

Under the given approximations, the reset can be simplified to a single reset pulse at the beginning of the PWM period:

$$r(t) = \begin{cases} 1 & \text{for} \quad 0 \le t \le t_r \\ 0 & \text{else} \end{cases}, \tag{26}$$

and with a narrow timing $t_r \to 0$. In particular, Figure 8 shows the trigger signal and the output of the integrator stage.

In the simplified approach, the effect of the resistance R_Σ is considered small compared to the inductive component [25]. Under this consideration, the ratio between R_Σ and L_d can be considered small and therefore Equation (9) can be linearized by applying the Taylor expression and truncating it at the first term:

$$e^{-\frac{R_\Sigma}{L_d}t} \approx 1 - \frac{R_\Sigma}{L_d}t. \tag{27}$$

By applying assumption (27) on the current ripple Equation (9) (For sake of brevity, only the rising part of the current ripple is shown, the falling part can be derived in a similar way.)

$$i_s(t) \approx i_s(t_s^+) + (\frac{U_{DC}}{R_\Sigma} - i_s(t_s^+))\frac{R_\Sigma \cdot t}{L_d} \qquad \text{for} \qquad 0 \le t \le \alpha \cdot t_{pwm}, \tag{28}$$

the current ripple is considered linear instead of being exponentially shaped. The offset removing stage removes the fundamental component from the sensed current:

$$\tilde{i}_s(t) \approx (\frac{U_{DC}}{R_\Sigma} - i_s(t_s^+))\frac{R_\Sigma \cdot t}{L_d} \qquad \text{for} \qquad 0 \le t \le \alpha \cdot t_{pwm}. \tag{29}$$

In order to simplify the mathematical treatment and implementation effort, it is assumed that the current ripple has low contribution to the total current. This is usually desired in practical implementations in order to avoid significant perturbations of the produced force caused by current ripples. Therefore, it can be written that the current ripple has negligible influence on the mean value

of the current: $i_s(t_s^+) \approx i_{s,m}$. Furthermore, by limiting the current dynamic under the assumption of a linear relationship between mean current $i_{s,m}$ and mean voltage u_m [25]:

$$i_s(t_s^+) \approx i_{s,m} \approx \frac{u_m}{R_\Sigma} = \frac{2U_{DC}(\alpha - 0.5)}{R_\Sigma}, \tag{30}$$

the expression of the current ripple shown in Equation (28) can be simplified:

$$\bar{i}_s(t) \approx \frac{2U_{DC}}{L_d} \cdot (1 - \alpha) \cdot t. \tag{31}$$

It is visible that the influence of the resistance R_Σ disappears. The maximum amplitude of the current ripple occurs at the time $t_{pwm} \cdot \alpha$ and therefore the function value of Equation (31) at this time instant can be expressed as:

$$\bar{i}_s(t_{pwm} \cdot \alpha) \approx \frac{2U_{DC}}{L_d} \cdot (1 - \alpha) \cdot t_{pwm} \cdot \alpha. \tag{32}$$

The current ripple with its first order approximation shown in Equation (27) resembles a triangle, whose integral value at the time t_e^- can be calculated as [25]:

$$I(t_e^-) \approx \frac{1}{2} \cdot t_{pwm} \cdot \bar{i}_s(t_{pwm} \cdot \alpha) = \frac{U_{DC}}{L_d} \cdot \alpha(1 - \alpha) \cdot t_{pwm}^2. \tag{33}$$

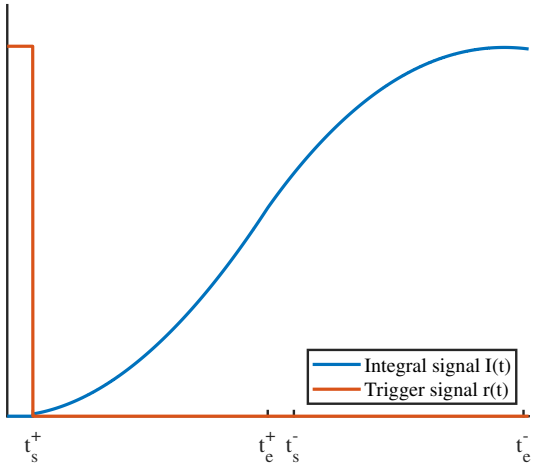

Figure 8. Integral obtained by the IDIM circuit for the simplified IDIM technique (blue), trigger signal $r(t)$ (red) as well as time instants, exemplary shown for $\alpha = 0.5$.

Finally, the inductance can be estimated by:

$$L_d \approx \frac{U_{DC}}{I(t_e^-)} t_{pwm}^2 \cdot \alpha \cdot (1 - \alpha). \tag{34}$$

It is visible that this technique requires one DC link voltage measurement and one measurement of the integrator circuit per each PWM period. Moreover, the inductance can be estimated by solving one closed equation. Thus, it can be considered that this method requires less sampling and computational effort with respect to the oversampling approaches. Nevertheless, the assumptions made during the mathematical derivation do not allow high dynamic operation.

3.3. Oversampling Approach

As mentioned earlier, many works [18–22] make use of an oversampled current and voltage measurement in order to estimate the inductance with a high noise robustness. Those methods take a number of N samples per each PWM period and obtain a data set of time, voltages, and currents:

$$\underline{t} = [t_s^+ ... t_e^+ \; t_s^- ... t_e^-], \tag{35}$$

$$\underline{u} = [u(t_s^+) ... u(t_e^+) \; u(t_s^-) ... u(t_e^-)], \tag{36}$$

$$\underline{i_s} = \underbrace{[i_s(t_s^+) ... i_s(t_e^+) \; i_s(t_s^-) ... i_s(t_e^-)]}_{\text{N Samples}}. \tag{37}$$

Taking the measurements after a short time t_r after a switching instant ensures that transients coming from parasitic components and from the current sensor are not considered during the estimation process [21,22]. Based on the obtained data set, the techniques either calculate numerically the flux, from which the inductance can be obtained [18,19], or identify the actuator inductance by means of least-mean squares (LMS) approaches [21,22]. For sake of brevity, those techniques will not be explained here in detail. In the following sections, the approach from [22] is used for inductance estimation. This work uses a LMS approach for the robust identification of the current ripple slopes, from which the inductance is estimated, with a number of 1600 samples per PWM period at a PWM frequency of 500 Hz. It therefore serves as a good representative method in this work. For further details, reference is made to [22].

4. Experimental Results

In order to evaluate the performance of the discussed approaches in terms of noise robustness and accuracy, an experimental test-bench consisting of a high precision linear positioning table, a dedicated electronics from the Laboratory of Actuation Technology and a mechanical coupling to the actuator is used, as shown in Figure 9. The working principle of the solenoid actuator is shown in Figure 10.

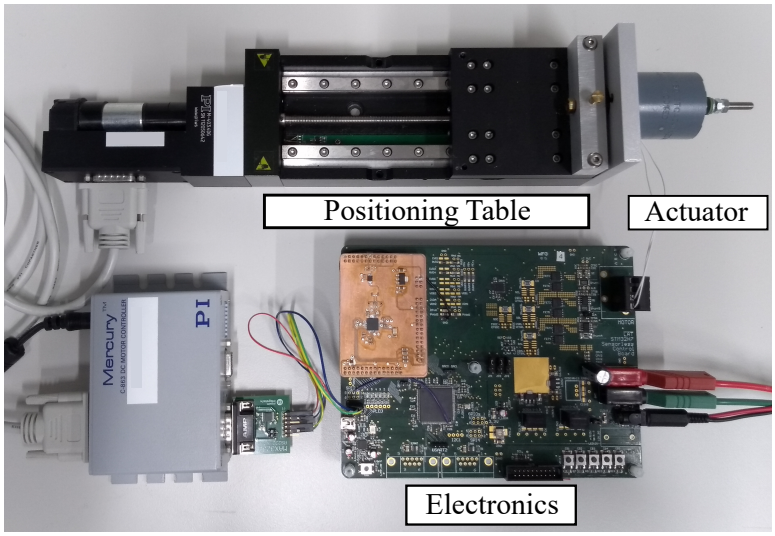

Figure 9. Experimental test-bench including positioning table, electronics, and test solenoid.

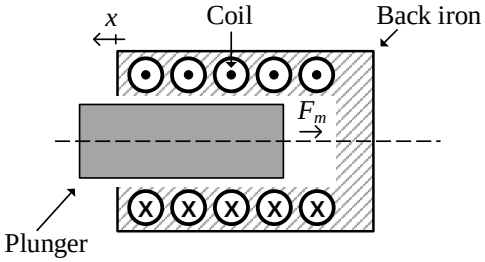

Figure 10. Schematic figure of the solenoid actuator consisting of plunger, coil and back-iron. The reluctance force generated in the actuator is denoted by F_m.

In particular, the positioning table M403.4DG from Physics Instruments [30] allows the positioning of the actuator and the measurement of the actuator position within a range of 10 cm with a minimum step size of 200 nm. The table is able to block the actuator at a certain position with forces up to 50 N. This table is connected to a dedicated electronics that consists of a switching power electronics, a STM32H7 microcontroller with 16 bit AD converters and a dedicated electronics for the IDIM technique. In particular, an AD8418 current sensor from Analog devices [31] with 250 kHz bandwidth is used for current measurement. The discussed inductance estimation approaches are implemented in the microcontroller using floating-point arithmetic. Moreover, a current controller is tuned and implemented accordingly, guaranteeing a constant current even under variable DC link voltage and increasing resistance R_Σ due to self-heating or due to the presence of a back-EMF. The actuator under test is an industrial switching solenoid from the type GTC A 40 from Magnet-Schulz Memmingen [32]. Its parameters and nominal values are listed along with the used settings of the IDIM technique in Table 1.

Table 1. Parameters of the used test solenoid as well as settings of the IDIM technique.

Parameter	Value
Nominal Voltage	24 V
Nominal Power	12.9 W
Nominal Resistance R_s	44.6 Ω
Nominal Stroke	8 mm
Max. Force	34.8 N
PWM frequency	500 Hz
Reset time t_r	50 µs
Integration gain	0.015 1/µs

Based on the mean electrical time constant of the actuator $\tau_{el} = 8.34$ ms, a PWM frequency of 500 Hz is chosen in order to produce a measurable current ripple and avoid saturation of the inductance over frequency. Figure 11 shows the experimental measurement of the analog signals in the IDIM circuitry. The applied PWM voltage causes a considerable current ripple, which has significant disturbances at the PWM switching instants due to the limited bandwidth of the current sensor and due to parasitic capacitances. Two different settings of the trigger signal $r(t)$ as well as the corresponding integrator outputs are shown: the trigger signal of the IDIM technique expressed by Equation (13) and the trigger signal of the simplified IDIM technique shown in Equation (26).

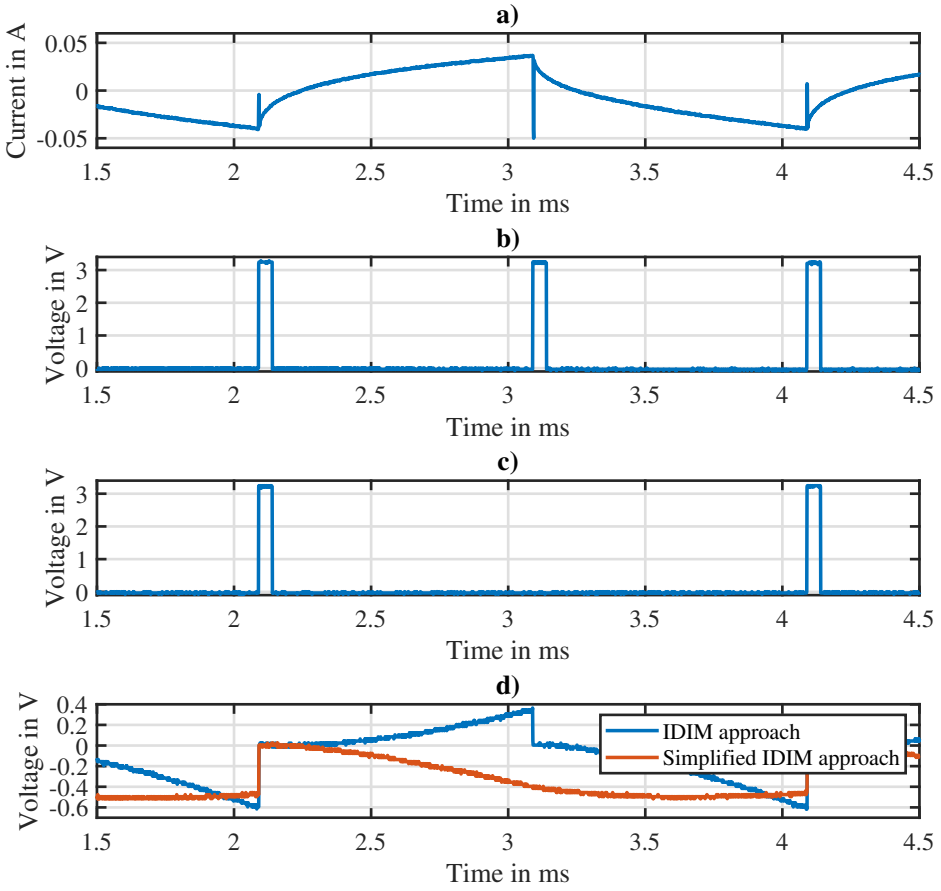

Figure 11. Measurements of the analog signals of the IDIM circuitry, (**a**) sensed current signal, (**b**) trigger signal $r(t)$ in case of the IDIM approach, (**c**) trigger signal $r(t)$ in case of the simplified IDIM approach, (**d**) resulting output of the integrator circuit in case of the IDIM approach (blue) and the simplified IDIM approach (red).

4.1. Noise Power of the Discussed Approaches

As mentioned before, most state-of-the art works increase the signal-to-noise ratio significantly by making an oversampled current measurement and by using least-mean squares algorithms with the demerit of increased computational effort and increased sampling effort. The IDIM technique aims to avoid an oversampled current measurement by reducing the noise level before sampling, thereby decreasing the sampling and computational effort. In the following, the inductance estimation performance of the IDIM approaches will be compared to an oversampling approach (OS) in terms of convergence and noise power. Note that no reference inductance value is available for comparison due to the lack of a general approach of exciting and estimating differential inductances at different working points. The noise power P_n is defined as follows:

$$P_n = \frac{1}{L}\Sigma_{i=1}^{L} n(i)^2 \tag{38}$$

where L is the length of the signal vector and $n(i)$ is the noise of the actual signal value. The noise is obtained by subtracting the actual signal value from the mean value of the entire signal vector [33].

Figure 12 shows the estimated inductance in case the actuator is at zero mean current and is fully opened (x = 8 mm). The noise power of the IDIM technique, the simplified IDIM technique as well as the oversampling approach with different numbers of samples per PWM period are shown and

compared. Oversampling approaches exceeding 1000 samples per PWM period are not considered here, since the microcontroller reaches it computational limits. Moreover, an experiment with the oversampling method with 50 samples per PWM period failed due to the divergence of the algorithm. It can be seen that the simplified IDIM technique achieves with -48.5 dB a slightly lower noise power than the oversampling approach with 100 samples per PWM period. The IDIM technique shows a lower noise power with -51.7 dB. Oversampling approaches with more samples per PWM period achieve considerably smaller noise powers. Nevertheless, the techniques are affected by biases, which change significantly depending on the number of used samples. This might be due to the fact that the oversampling approaches are not converging properly when a sufficient number of samples is not given. In particular, the simplified IDIM technique shows a remarkable bias in the inductance estimate. This is due to the assumption of a linearized current ripple made by Equation (27).

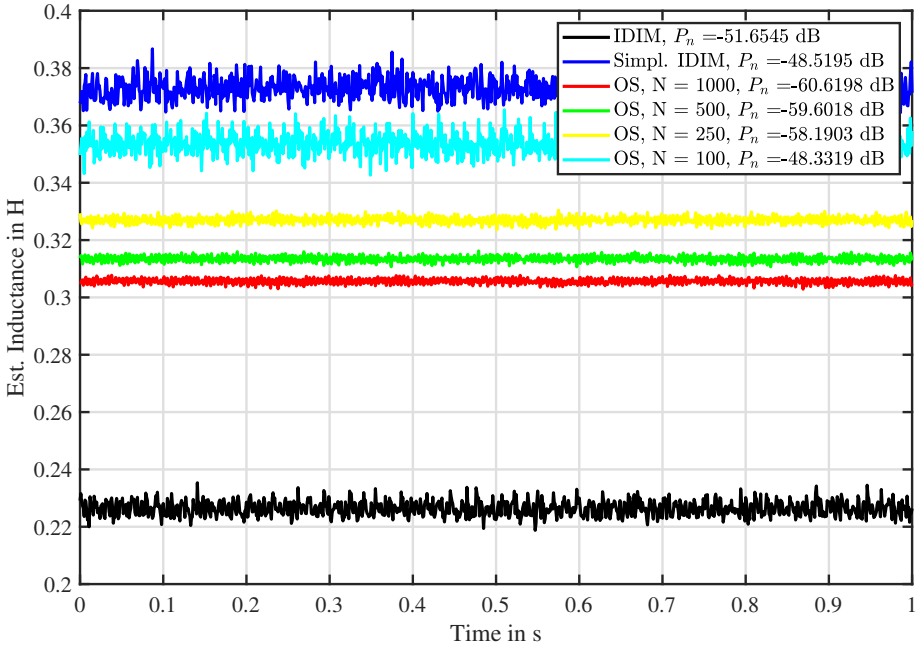

Figure 12. Comparison of the noise power obtained by the different approaches when the actuator is fully opened and under zero mean current conditions.

The experiment is repeated in the case the actuator is driven with full mean current and is closed (x = 0 mm), as shown in Figure 13. In this experiment, the IDIM technique shows a noise power in the range of -59.1 dB, outperforming the oversampling approach with 250 samples. The simplified IDIM technique performs slightly better with a noise power of -60.8 dB. Nevertheless, oversampling approaches with more than 250 samples exhibit a lower noise power. Similarly to the results of Figure 12, all estimates differ in their bias. In the case of the oversampling techniques, the bias is strictly dependent on the number of samples, which indicates that those techniques need a sufficient number of samples in order to converge. In the case of the actuator under full mean current, this dependence gets more significant. This is due to the fact that the contribution of the current ripple to the total current inside the actuator decreases with increasing mean current. Thus, its processing is more likely to be influenced by biases during the estimation processes. The bias between the IDIM technique and its simplified implementation can be explained by the linear assumption made by Equation (27).

It can be seen that the IDIM technique has less noise power compared to the oversampling approaches with a number of up to 100 samples in case of the actuator without current and up to 250 samples in case of the driven actuator. Given the sampling effort and computational effort, which is needed for obtaining a good noise power with the oversampling approaches, the IDIM technique shows a good trade-off between noise power and needed effort.

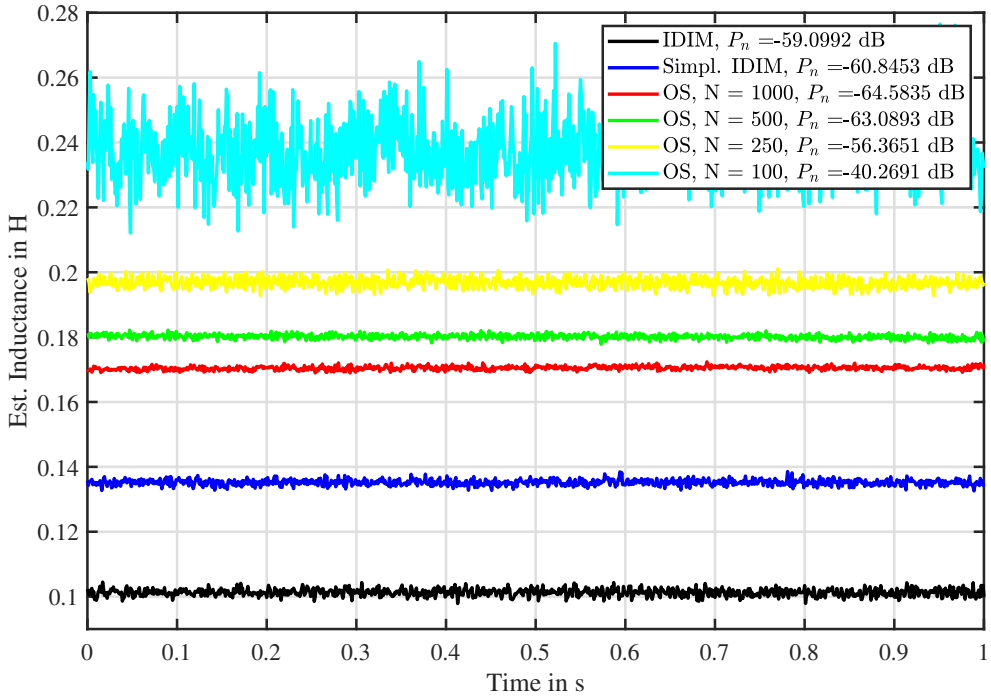

Figure 13. Comparison of the noise power obtained by the different approaches when the actuator is fully closed and full mean current is flowing.

4.2. Inductance Characteristic of the Actuator under Testing

In the following, the inductance characteristic of the actuator under test will be identified using the IDIM technique. With the help of the above-mentioned test-bench, it is possible to obtain the differential inductance of the actuator in the entire position and current range. Those measurements are shown in Figure 14 and for better visibility in Figure 15 for fixed positions at varying currents and in Figure 16 for fixed currents at varying positions. The measurements are obtained by averaging the inductance estimate over 200 values at each working point in order to increase visibility and comprehension of the measurements.

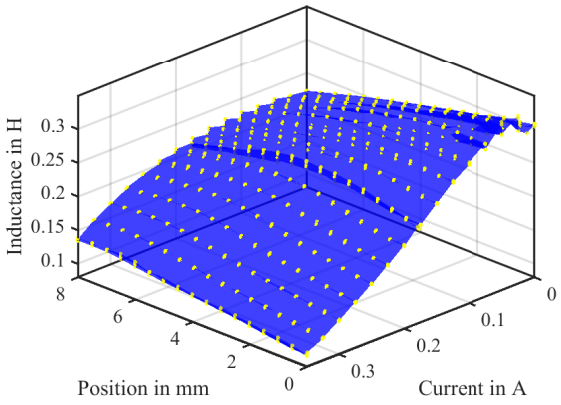

Figure 14. Obtained inductance characteristic when the IDIM approach is used. Inductance characteristic is shown over the entire position and current range. The yellow dots indicate the measured data points while the blue surface illustrates the interpolated data.

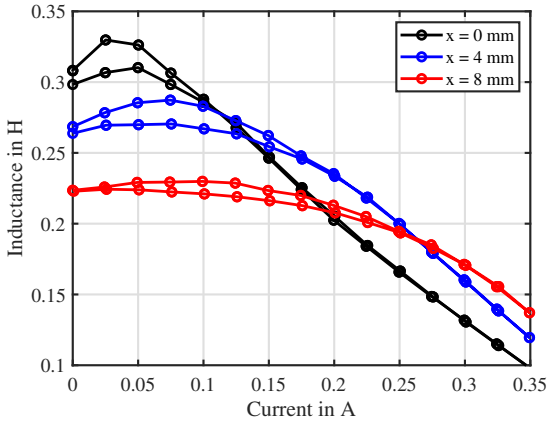

Figure 15. Identified inductance variation over changing current at three different fixed positions. The dependency is strongly hysteretic.

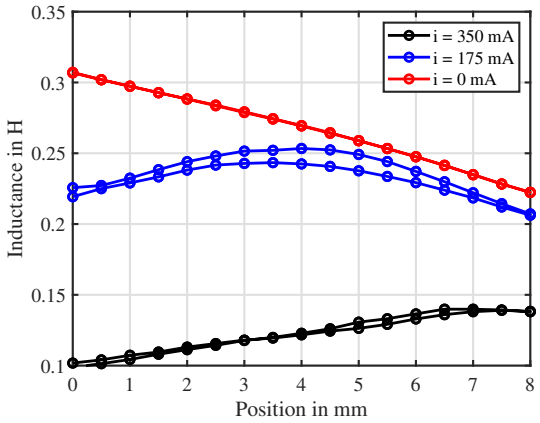

Figure 16. Identified inductance variation over changing position at three different fixed currents. The dependency is slightly hysteretic, in particular for middle range currents.

The identified inductance characteristic exhibits a remarkable hysteresis over position and current due to the presence of a hysteretic plunger and back-iron material [34] (p. 32). At higher currents, the material shows no hysteresis anymore and goes into saturation [34] (p. 21). This resembles the B–H-curve of the plunger material. Indeed, removing the plunger from the coil effectively increases the inductance at higher currents [34] (p. 21).

For the purpose of sensorless end-position detection in a switching actuator, only the red curve, indicating the case of zero mean current, and the black curve, representing full mean current, are of particular interest in Figure 16. The curve representing the zero mean current condition shows no hysteresis and can be considered anhysteretic. The curve describing the full mean current condition shows a slight hysteresis, which is going to be neglected for a simplified modeling. The obtained pre-filtered measurement curves are inverted for means of position estimation and the measurement points are fitted with polynomials of the 4th order.

4.3. Validation of the Use Case Scenario: Sensorless End-Position Detection for Switching Actuators

In the following, the discussed approaches are validated in the use case scenario of a sensorless end-position detection for switching actuators. The fitted polynomials mentioned in the section above are implemented for the purpose of position estimation. During the validation experiment, the positioning table is used to move the plunger in a quasi-static manner over the entire position range of the actuator. For the application of sensorless end-position detection in a switching application, two cases are shown: the actuator is without current (i = 0 A), shown in Figure 17, and the actuator is

under full mean current (i = 350 mA), illustrated in Figure 18. In those figures, the position estimation obtained by the IDIM method, the simplified IDIM method, and the oversampling methods with 100 and 250 samples are compared to the position measurement of the high-precision position table. For the sake of brevity, only the oversampling approaches with 100 and 250 samples are shown since their noise power resembles the ones of the IDIM techniques. Note that, in this experiment, no low-pass filtering is applied to the measurements, allowing to compare the estimation performance directly.

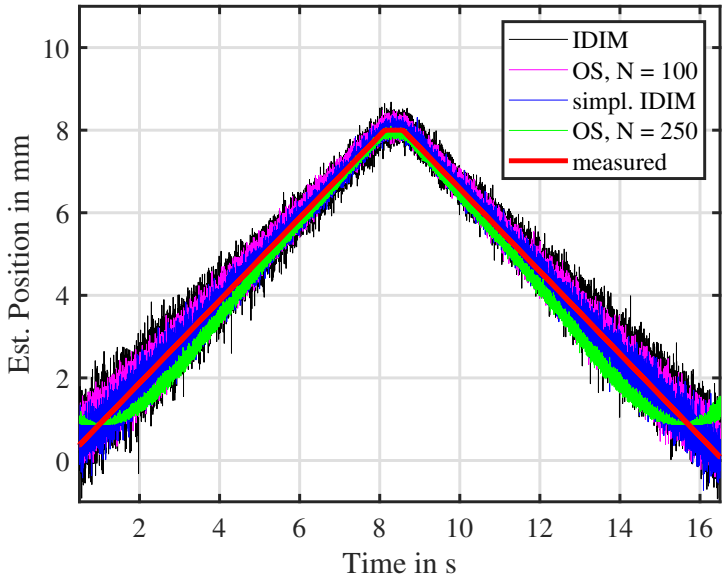

Figure 17. Performance of the obtained sensorless end-position estimator: results are obtained by the IDIM (black), the simplified IDIM approach (blue) and the oversampling approaches with 100 samples (magenta) and 250 samples (green) compared to the position obtained by the high resolution positioning table (red). Results are shown when the actuator has a zero mean current ($i = 0$).

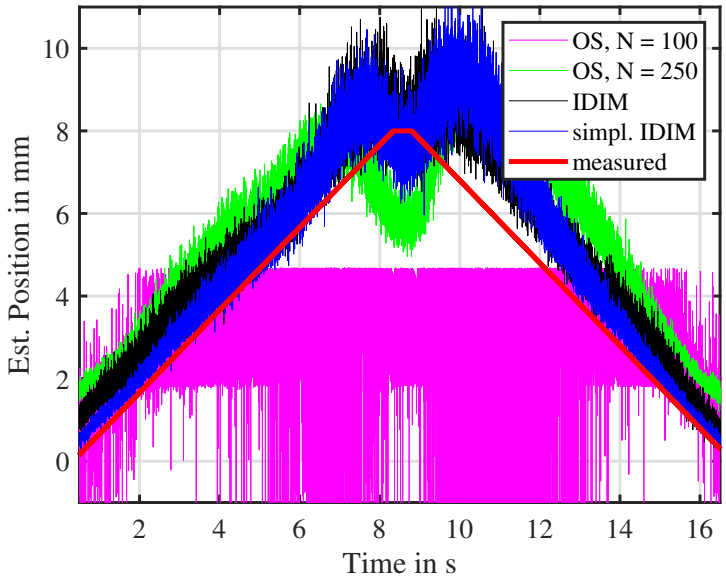

Figure 18. Performance of the obtained sensorless end-position estimator: results are obtained by the IDIM (black), the simplified IDIM approach (blue) and the oversampling approaches with 100 samples (magenta) and 250 samples (green) compared to the position obtained by the high resolution positioning table (red). Results are shown when the actuator is driven with full mean current ($i = 350$ mA).

From both experiments, it can be seen that the position estimated by the (simplified) IDIM method follows the measured position in a clear way. In the case of the actuator without mean current, shown in Figure 17, the oversampling approaches show similar performance as the IDIM approaches. The oversampling approach with 250 sample tracks the measured position, but with estimation errors at positions smaller than 1.5 mm. In the case of the actuator under full mean current, shown in Figure 18, the oversampling approach with 100 samples fails to converge to the measured position while the approach with 250 samples converges and tracks the position. All techniques present a considerable estimation error in the case that the actuator is driven with full mean current due to the negligence of the actuator hysteresis, as shown in Figure 18.

Because of that hysteretic behavior, whose modeling is not within the scope of this work, only the results from Figure 17 are discussed. The position estimates of the different techniques are affected by noise, whose amplitude changes according to the used estimation technique: the simplified implementation of the IDIM technique shows a lower noise amplitude than the IDIM technique and the oversampling approach with 100 samples. The oversampling approach with 250 samples shows the lowest noise amplitude due to a high number of used samples. Table 2 quantifies and compares the mean and maximum errors of the techniques with the result that the simplified IDIM technique achieves the lowest mean and absolute error for the purpose of sensorless end-position detection. The good performance of the simplified IDIM technique in terms of measurement noise is due to the fact that its estimation Equation (34) does not need to calculate current differences, unlike the estimation Equation (25) of the IDIM technique. Calculating differences of noisy signals increases the noise level of the result.

Table 2. Mean and maximum absolute error of the estimated position obtained by different techniques in case the actuator has zero mean current.

Technique	Mean Error	Max. Absolute Error
IDIM approach	0.13 mm	2.11 mm
simplified IDIM approach	−0.02 mm	1.28 mm
OS approach, N = 100	−0.07 mm	1.34 mm
OS approach, N = 250	−0.20 mm	1.78 mm

5. Conclusions

In this work, a thorough mathematical analysis of current ripples inside electromagnetic actuators when driven with switching electronics is conducted taking into account the presence of eddy currents and parasitic capacitances. The results of this analytical as well as numerical analysis prove that the presence of these effects has a significant influence on the current ripple especially at the switching time instants of the PWM driving voltage.

The presented Integrator-Based Direct Inductance Measurement (IDIM) technique is improved with respect to its previous formulations by exploiting the preceding analysis on the current ripples and compared to oversampling approaches. The comparative study conducted on an industrial solenoid actuator has shown that the IDIM technique provides, under certain conditions, similar performance in terms of noise as oversampling techniques, while requiring a much lower number of measured samples. Thus, both measurement and computational efforts are reduced, making the IDIM technique more suitable for application to low-cost electromagnetic actuators, where high-speed AD converters and high performance computation units, such as FPGAs, would considerably increase costs.

Finally, a use case scenario involving sensorless end-position detection is considered. This is, indeed, a typical application for switching valves, relays, and solenoid actuators. The experimental validation of a position estimator based on the IDIM technique shows good noise robustness and position tracking performance. Nevertheless, the position estimator shows a remaining deviation of the estimated position when the actuator operates at high currents. This is due to the negligence of hysteresis in the mathematical model of the inductance characteristic. This limitation is common to

all the techniques considered in this work and, therefore, the identification and compensation of the hysteretic behavior of such actuators represent an important aspect for future research activities.

6. Patents

The IDIM method has been submitted for patenting and references can be found in [26].

Author Contributions: Conceptualization, N.K., E.G., and M.N.; Methodology, N.K. and E.G.; Software, N.K.; Validation, N.K.; Formal analysis, N.K.; Investigation, N.K.; Writing—original draft preparation, N.K.; Writing—review and editing, N.K., E.G., and M.N.; Funding acquisition, M.N. All authors have read and agreed to the published version of the manuscript.

Funding: This research received no external funding.

Acknowledgments: We acknowledge support by the Deutsche Forschungsgemeinschaft (DFG, German Research Foundation) and Saarland University within the funding programme Open Access Publishing.

Conflicts of Interest: The authors declare no conflict of interest.

References

1. Kramer, T.; Weber, J.; Pflug, G.; Harnisch, B. Intelligent Condition Monitoring of Bi-stable Process Valves. In Proceedings of the Fluid Power Networks: Proceedings: 11th International Fluid Power Conference, Aachen, Germany, 19–21 March 2018.
2. Gadyuchko, A.; Kireev, V.; Rosenbaum, S. Magnetic Precision Measurement for Electromagnetic Actuators. In Proceedings of the 10 ETG/GMM-Symposium Innovative Small Drives and Micro-Motor Systems, Cologne, Germany, 14–15 September 2015.
3. Braun, T.; Reuter, J.; Rudolph, J. Sensorlose Positionsregelung eines hydraulischen Proportional-Wegeventils mittels Signalinjektion. *Automatisierungstechnik* **2017**, *65*, 260–269. [CrossRef]
4. Richter, S. *Ein Beitrag zur Integration von Maßnahmen der Funktionalen Sicherheit in Einen Geregelten Elektrohydraulischen Antrieb für Stationäre Anwendungen*; Fluidmechatronische Systeme; Shaker: Herzogenrath, Germany, 2016.
5. Benjak, O.; Gerling, D. Review of position estimation methods for IPMSM drives without a position sensor part I: Nonadaptive methods. In Proceedings of the XIX International Conference on Electrical Machines (ICEM 2010), Rome, Italy, 6–8 September 2010; pp. 1–6. [CrossRef]
6. Schrödl, M. Sensorless control of AC machines at low speed and standstill based on the "INFORM" method. In Proceedings of the IAS '96, Conference Record of the 1996 IEEE Industry Applications Conference Thirty-First IAS Annual Meeting, San Diego, CA, USA, 6–10 October 1996; Volume 1, pp. 270–277. [CrossRef]
7. Jansen, P.; Lorenz, R. Transducerless position and velocity estimation in induction and salient AC machines. *IEEE Trans. Ind. Appl.* **1995**, *31*, 240–247. [CrossRef]
8. Corley, M.; Lorenz, R. Rotor position and velocity estimation for a salient-pole permanent magnet synchronous machine at standstill and high speeds. *IEEE Trans. Ind. Appl.* **1998**, *34*, 784–789. [CrossRef]
9. Linke, M.; Kennel, R.; Holtz, J. Sensorless speed and position control of synchronous machines using alternating carrier injection. In Proceedings of the IEEE International Electric Machines and Drives Conference, Madison, WI, USA, 1–4 June 2003; Volume 2, pp. 1211–1217. [CrossRef]
10. Eyabi, P.B. Modeling and Sensorless Control of Solenoidal Acutators. Ph.D. Thesis, The Ohio State University, Columbo, OH, USA, 2003.
11. Braun, T.; Reuter, J.; Rudolph, J. Observer Design for Self-Sensing of Solenoid Actuators with Application to Soft Landing. *IEEE Trans. Control Syst. Technol.* **2018**, 1–8. [CrossRef]
12. Kučera, L. Zur Sensorlosen Magnetlagerung. Ph.D. Thesis, Eigenössische Technische Hochschule Zürich, Zürich, Switzerland, 1997.
13. Ganev, E. Sensorless Position Measurement Method for Solenoid-Based Actuation Devices Using Inductance Variation. U.S. Patent US20070030619A1, 8 February 2007.

14. Pawelczak, D.; Trankler, H.R. Sensorless position control of electromagnetic linear actuator. In Proceedings of the 21st IEEE Instrumentation and Measurement Technology Conference (IEEE Cat. No.04CH37510), Como, Italy, 18–20 May 2004; pp. 372–376. [CrossRef]
15. Rahman, M.; Cheung, N.; Lim, K. A sensorless position estimator for a nonlinear solenoid actuator. In Proceedings of the IECON '95—21st Annual Conference on IEEE Industrial Electronics, Orlando, FL, USA, 6–10 November 1995; Volume 2, pp. 1208–1213. [CrossRef]
16. Rahman, M.; Cheung, N.; Lim, K.W. Position estimation in solenoid actuators. *IEEE Trans. Ind. Appl.* **1996**, *32*, 552–559. [CrossRef]
17. Li, L.; Shinshi, T.; Shimokohbe, A. State Feedback Control for Active Magnetic Bearings Based on Current Change Rate Alone. *IEEE Trans. Magn.* **2004**, *40*, 3512–3517. [CrossRef]
18. Dülk, I.; Kovácsházy, T. Modelling of a linear proportional electromagnetic actuator and possibilities of sensorless plunger position estimation. In Proceedings of the 2011 12th International Carpathian Control Conference (ICCC), Velke Karlovice, Czech Republic, 25–28 May 2011; pp. 89–93. [CrossRef]
19. Dülk, I.; Kovácsházy, T. Sensorless position estimation in solenoid actuators with load compensation. In Proceedings of the 2012 IEEE International Instrumentation and Measurement Technology Conference Proceedings, Graz, Austria, 13–16 May 2012; pp. 268–273. [CrossRef]
20. Glück, T.; Kemmetmüller, W.; Tump, C.; Kugi, A. A novel robust position estimator for self-sensing magnetic levitation systems based on least squares identification. *Control. Eng. Pract.* **2011**, *19*, 146–157. [CrossRef]
21. Glück, T. *Soft Landing and Self-Sensing Strategies for Electromagnetic Actuators*; Number 18 in Modellierung und Regelung Komplexer Dynamischer Systeme; Shaker: Aachen, Germany, 2013.
22. Ahmed, S.; Van-Duc, D.; Koseki, T. Electromagnetic levitation control with sensorless large air gap detection for translational motion application using measured current-ripple slope. In Proceedings of the IECON 2016—42nd Annual Conference of the IEEE Industrial Electronics Society, Florence, Italy, 23–26 October 2016; pp. 4275–4280. [CrossRef]
23. Pawelczak, D.R. Nutzung Inhärenter Messeffekte von Aktoren und Methoden zur Sensorlosen Positionsmessung im Betrieb. Ph.D. Thesis, Bundeswehr University Munich, Munich, Germany, 2006.
24. Noh, M.; Maslen, E. Self-sensing magnetic bearings using parameter estimation. *IEEE Trans. Instrum. Meas.* **1997**, *46*, 45–50. [CrossRef]
25. Koenig, N.; Grasso, E.; Merl, D.; Nienhaus, M. A Position Estimation Method for Single-Phase Electrical Machines Without Injecting Extra Test Pulses. In Proceedings of the 2018 IEEE 9th International Symposium on Sensorless Control for Electrical Drives (SLED), Helsinki, Finland, 13–14 September 2018; pp. 42–47. [CrossRef]
26. Grasso, E.; König, N.; Nienhaus, M.; Merl, D. Verfahren und Vorrichtung zur Bestimmung Einer Induktivitätsangabe Eines Elektromagnetischen Aktuators. EP3544173A1, 25 September 2019.
27. Koenig, N.; Anzelmi, G.; Naso, D.; Nienhaus, M.; Grasso, E. An Improved IDIM Technique for Sensorless Control of Single-Phase Electromagnetic Drives. In Proceedings of the 2019 IEEE 10th International Symposium on Sensorless Control for Electrical Drives (SLED), Turin, Italy, 9–10 September 2019; pp. 1–6. [CrossRef]
28. Fraga, E.; Prados, C.; Chen, D.X. Practical model and calculation of AC resistance of long solenoids. *IEEE Trans. Magn.* **1998**, *34*, 205–212. [CrossRef]
29. Koenig, N.; Grasso, E.; Nienhaus, M. Robust Electrical and Mechanical Parameter Identification of Low-Power PMSMs. In Proceedings of the 11th GMM/ETG-Symposium, Innovative Small Drives and Micro-Motor Systems, Saarbruecken, Germany, 27–28 September 2017.
30. Physik Instrumente (PI) GmbH. M-403 Linear Stage. Available online: https://www.physikinstrumente.com/en/products/linear-stages/stages-with-stepper-dc-brushless-dc-bldc-motors/m-403-precision-translation-stage-701750/ (accessed on 13 January 2020).
31. Analog Devices. AD8418 Datasheet and Product Info | Analog Devices. Available online: https://www.analog.com/en/products/ad8418.html (accessed on 13 January 2020).
32. Magnet Schultz Memmingen. Single Acting Solenoids Type G TC A. Available online: https://www.magnet-schultz.com/en/solenoids/single-acting-solenoids-type-g-tc-a/ (accessed on 13 January 2020).

33. Kieser, R.; Reynisson, P.; Mulligan, T.J. Definition of signal-to-noise ratio and its critical role in split-beam measurements. *ICES J. Mar. Sci.* **2005**, *62*, 123–130. [CrossRef]
34. Kallenbach, E.; Eick, R.; Quendt, P.; Ströhla, T.; Feindt, K.; Kallenbach, M.; Radler, O. (Eds.) *Elektromagnete: Grundlagen, Berechnung, Entwurf und Anwendung; mit 38 Tabellen*, 4th ed.; Vieweg + Teubner: Wiesbaden, Germany, 2012; ISBN 978-3-8348-0968-1.